

# Dual Phase LLC Resonant Converter With Variable Frequency Zero Circulating Current Phase-Shift Modulation for Wide Input Voltage Range Applications

Asif Mustafa<sup>1</sup> and Saad Mekhilef<sup>2</sup>, *Senior Member, IEEE*

**Abstract**—This article proposes a novel dual phase LLC resonant converter with an improved variable frequency-based zero circulating current phase-shift modulation scheme for wide input voltage applications. The presented topology employs a six-switch dual active bridge with two output ports reducing the voltage stress across upper and lower switches to half of the input voltage. The proposed modulation scheme is a three-variable control that enables the converter to operate with increased voltage gain range under all input voltage and loading conditions. Variable frequency control leads to the soft switching operation of the switches connected to the primary side for all load ranges. The phase-shift control is used as power transfer control along with maintaining a constant output voltage under changing input voltage. Moreover, the duty cycle calculation based on load conditions helps in eliminating the reverse power flow especially under light-load conditions. To verify the proposed converter and modulation scheme, a 1.5-kW prototype with 210–400-V input and 80-V output is built and tested with a peak load efficiency of 96.7%.

**Index Terms**—LLC, resonant converter, reverse power flow (RPF), variable frequency phase shift modulation (VFPSM), zero voltage switching (ZVS).

## I. INTRODUCTION

DUAL active bridge (DAB) is drawing much interest pertaining to its appealing features such as excellent power transfer capability, galvanic isolation and protection, reliability,

Manuscript received March 3, 2020; revised May 22, 2020 and July 18, 2020; accepted August 5, 2020. Date of publication August 11, 2020; date of current version October 30, 2020. This work was supported in part by the University of Malaya, Malaysia, under grant Impact Oriented Interdisciplinary Research Grant (IIRG): IIRG011A-2019, in part by the Ministry of Higher Education, Malaysia, under Large Research Grant Scheme (LRGS): LR008-2019, and in part by the Ministry of International Trade and Industry (MITI), Malaysia, through MIDF under High Value Added and Complex Product Development and Market Program: GA016-2019. Recommended for publication by Associate Editor Y. Xing. (*Corresponding author: Saad Mekhilef.*)

Asif Mustafa is with the Power Electronics and Renewable Energy Research Laboratory, Department of Electrical Engineering, University of Malaya, Kuala Lumpur 50603, Malaysia (e-mail: asifmustafa65@gmail.com).

Saad Mekhilef is with the Power Electronics and Renewable Energy Research Laboratory, Department of Electrical Engineering, University of Malaya, Kuala Lumpur 50603, Malaysia, and also with the School of Software and Electrical Engineering, Faculty of Science, Engineering and Technology, Swinburne University of Technology, Victoria, VIC 3122, Australia (e-mail: saad@um.edu.my).

Color versions of one or more of the figures in this article are available online at <https://ieeexplore.ieee.org>.

Digital Object Identifier 10.1109/TPEL.2020.3015799

and high power density [1]. It can achieve zero voltage switching (ZVS) with the limitation of voltage gain to unity for all-load conditions [2], [3]. However, this feature suffers when the turn ratio of the transformer is not unity [4].

With the aim of extended gain and ZVS range, the resonant converters have been employed in [5]–[7] with improved efficiency. The series resonant dual active full bridge (FB) converter has been proposed in [8] using fixed frequency phase-shift modulation (FFPSM). The voltage gain of the converter has been limited to unity for ZVS achievement over entire load variation. As proposed in [9], the LLC BDC is operated at a fixed frequency with varying duty cycle calculated as per the required voltage gain. The additional inductor in secondary makes the converter operate at the cost of increased power loss. The proposed CLLC resonant converter in [10] employs pulse frequency modulation (PFM) for bidirectional power flow and has ZVS for entire load variation. A modified LLC resonant converter has been presented in [11] that splits the resonant inductor to extend the gain range; however, the two resonant circuits are not equally utilized with the switches under high voltage stress. In [12], a FB LLC circuit is combined with a dual-phase interleaved boost circuit sharing the same FB. In [13], a buck–boost converter is combined with the primary half bridge (HB). However, the required resonant components are bulky. Moreover, the duty cycle control is either limited to boost or a buck–boost converter. Therefore, the FB output rms voltage is pulse width modulated voltage (PMW). This influences the ZVS operation of MOSFETs and zero current switching (ZCS) of diodes. The three-level dc/dc LLC converters have been proposed in [14] and [15]. With additional capacitors and MOSFETs, the voltage stresses can be reduced. The voltage regulation range is also enhanced with more degrees of freedom in the control strategy.

Many researchers have focused on altering the secondary side to achieve higher voltage gain with narrow switching frequency range. The rectifier structures have been reconfigured in [16]–[20] as HB rectifier, FB rectifier, voltage doubler, and voltage-quadrupler rectifier. Nonetheless, the increased count of switches and conduction losses are the limitations of such structures. A secondary-side PWM has been proposed in [21] to increase the voltage gain range. However, the converter efficiency is degraded, and current stresses are increased due to asymmetrical operation under extreme regulation conditions.

In [22], the short-circuited (SC) secondary bridge has been presented in one of its operation modes. However, the SC time duration must be necessarily small to maintain the stability of the converter circuit. Moreover, the output voltage ripples and current stress through circuit elements have been increased.

For the sake of minimized reverse power flow (RPF), many control schemes have been proposed [23]–[25]. A triangle modulation (TRM) scheme has been employed in [26] to obtain reduced circulating current with ZCS behavior for the entire operating range. However, the feasibility of TRM is limited for the operation to gain more than unity. The dual phase shift (DPS), as proposed in [27], employs a phase shift between the legs of a bridge as that of phase shift between two bridges to eliminate the RPF. In order to deal with light-load efficiency issue in conventional DAB, a broad analysis of phase shift with PWM has been presented in [28]. The proposed extended phase shift (EPS) in [29] incorporates the duty cycle control to extend the ZVS range. Additionally, it resolves the RPF at input voltage side, when DAB is interconnected through a micro grid. However, the RPF elimination is limited to input side only. In [30], the proposed modulation is aimed at eliminating the circulating current to regulate the transferred power over the entire range with zero RPF at the output side, though the RPF exists at the input voltage side. An innovative semi-DAB converter has been suggested in [31] to eliminate RPF on the outside side with a reduced number of switches. It achieves ZVS for the entire operating range. Nevertheless, the power transmission is limited to unidirectional. In [32], the triple phase shift (TPS) employs two inner phase shift as compared to DPS. It is the most general modulation strategy. However, because of the increased number of switching stages, the general control strategy is needed to be optimized under all input voltage and load conditions.

The foremost contribution of this article is to propose a novel dual LLC resonant converter with an improved variable frequency zero circulating current phase-shift modulation (VFPSM-ZCC) aimed at eliminating the RPF under all load conditions for wide input voltage range applications. The proposed converter demonstrates the following advantages: 1) wide voltage gain range; 2) eliminates reverse power flow (RPF); 3) half input voltage stress on four MOSFETs; 4) voltage gain being independent of load conditions; and 5) squeezed switching frequency range. Consequently, the proposed LLC resonant converter makes up as an apt selection for renewable-based energy-systems in medium/high voltage applications.

## II. ANALYSIS OF THE PROPOSED CONVERTER OPERATION

### A. Proposed Topology

The circuit configuration of the proposed dual LLC resonant dc–dc converter for a wide input voltage range is shown in Fig. 1. It consists of high voltage side (HVS) and low voltage side (LVS) as in the primary and secondary side of the high-frequency transformer. With the aim of wide input voltage range and zero RPF in the converter, two LLC resonant tanks are series connected on HVS of the converter. The transformer leakage inductance ( $L_{lk}$ ) is used with an extra inductor ( $L_{ext}$ ) to constitute the resonant inductor ( $L_{r1}/L_{r2}$ ) of each LLC resonant tank. The

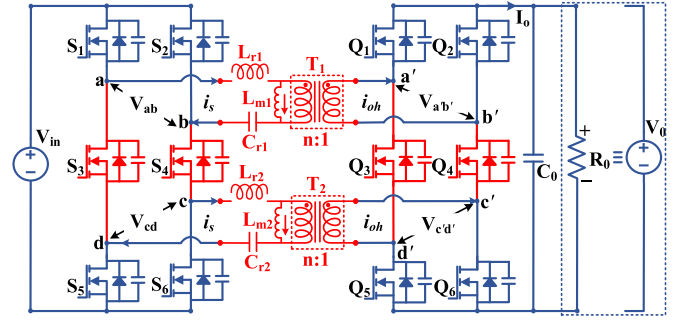


Fig. 1. Proposed bidirectional dual LLC resonant converter.

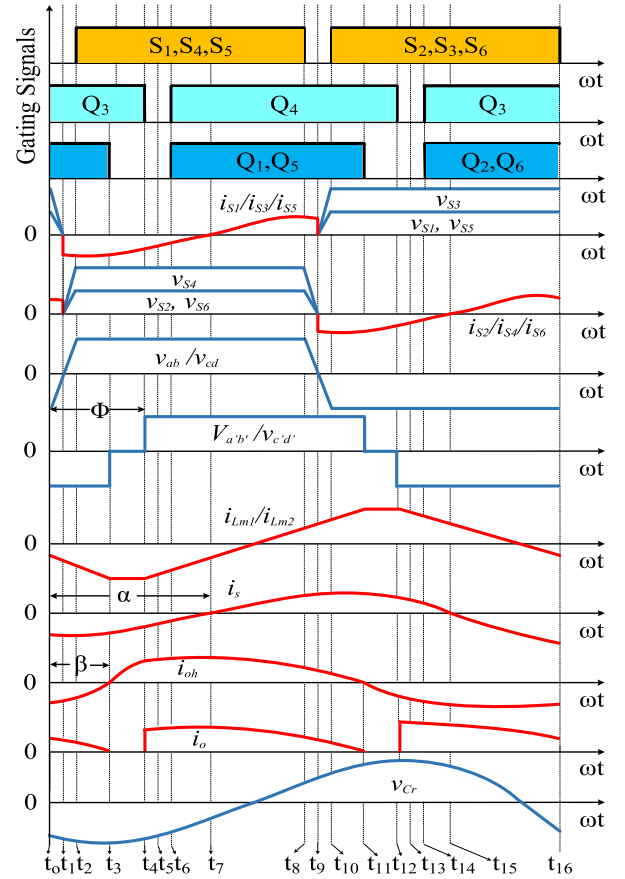


Fig. 2. Key operation waveforms of the proposed dual LLC resonant converter.

series resonance capacitor ( $C_{r1}/C_{r2}$ ) filters out the dc component from any reverse current that might hamper the saturation of the transformer. The transformers  $T_1$  and  $T_2$  having identical turn ratios ( $n_1 = n_2$ ) are series connected on both sides. Hence, the current flowing through the windings is always equal resulting in equal power distribution between the transformers. The output capacitor,  $C_0$ , is large enough to filter out the voltage ripples. The identical resonant tanks have the resonant parameters as,  $L_{r1} = L_{r2} = 0.5L_r$ ,  $C_{r1} = C_{r2} = 2C_r$ ,  $L_{m1} = L_{m2} = 0.5L_m$ , where  $L_r$ ,  $C_r$ , and  $L_m$  are the resonant parameters of the equivalent resonant tank.

The steady-state waveforms of the proposed converter are shown in Fig. 2. The six HVS switches  $S_1$ – $S_6$  operate with a fixed duty cycle of 50%. The switches  $S_1$ ,  $S_4$ , and  $S_5$ , are triggered

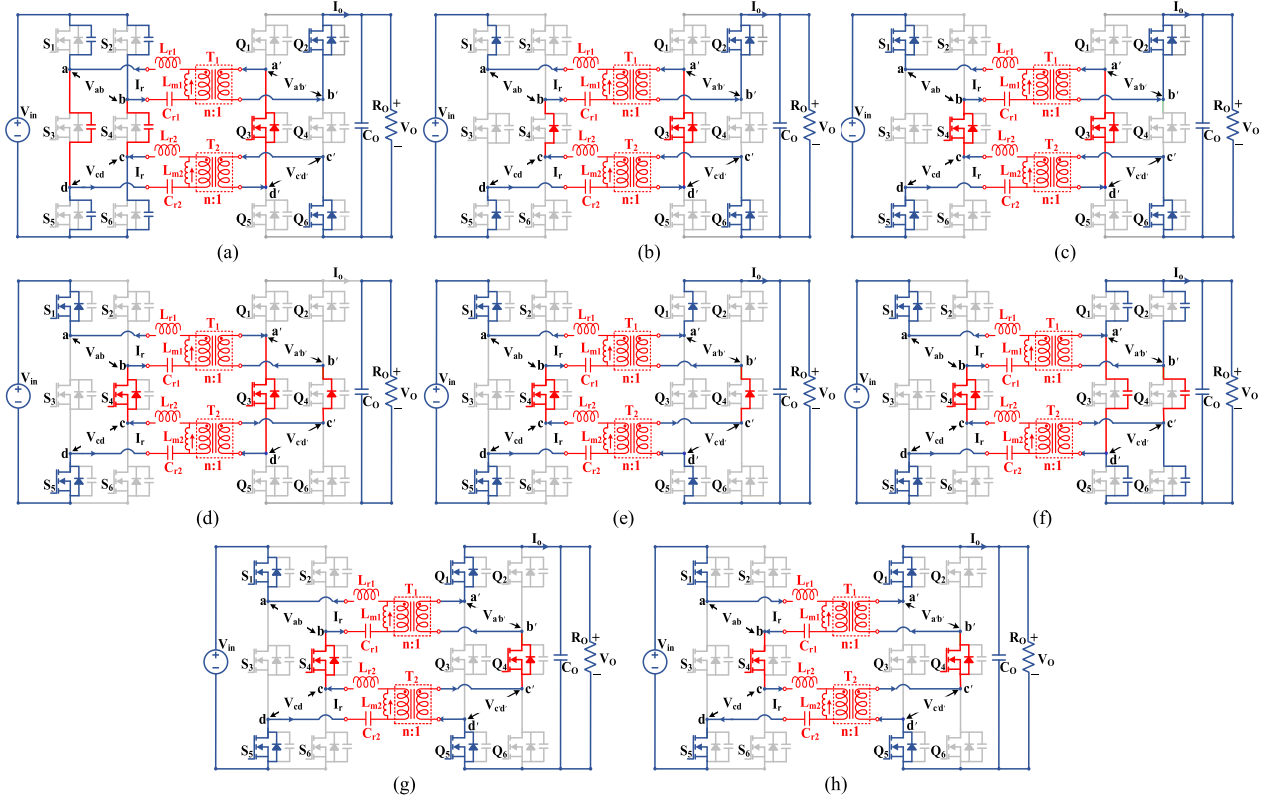


Fig. 3. Equivalent circuits for half switching cycle. (a)  $[t_0-t_1]$ . (b)  $[t_1-t_2]$ . (c)  $[t_2-t_3]$ . (d)  $[t_3-t_4]$ . (e)  $[t_4-t_5]$ . (f)  $[t_5-t_6]$ . (g)  $[t_6-t_7]$ . (h)  $[t_7-t_8]$ .

by the same gate signals, whereas,  $S_2$ ,  $S_3$ , and  $S_6$  are turned ON and OFF simultaneously. The voltage,  $V_{ab}$  between points  $a$  and  $b$  is half the input voltage  $V_{in}$ . In a similar manner,  $V_{cd}$  is half of the input voltage. The improved modulation technique constitutes of the varying duty cycle for the secondary switches along with frequency and phase-shift control. The switches  $Q_3$  and  $Q_4$  are triggered at 50% duty cycle in a complementary manner. The controller tracks the output current ( $I_0$ ) and inhibits it from going negative by triggering ON and OFF the switches  $Q_1$ ,  $Q_5$  and  $Q_2$ ,  $Q_6$  for less than 50% duty cycle. The improved phase-shift modulation strategy is employed for the control of reverse power flow. This reverse power becomes severe under light-load conditions reducing the converter efficiency. The phase-shift angle  $\varphi$  between the HVS and LVS switches is varied to control the output voltage and power flow in the converter. For a positive phase-shift angle, power flows from HVS to LVS. For the backward operation, the phase shift is reverse and the converter operates as series resonant converter. The single phase-shift (SPS) modulation as employed in [7] for backward mode of operation has been used in this article. The converter's power flow characteristics and ZVS range for backward operation are similar to series resonant converters [7]. The analysis has been done for the forward mode of operation.

### B. Operation Principles

The proposed converter operation in the forward power flow is elaborated in the subsequent part of the article. There are a total of 16 operation stages of the proposed LLC resonant

converter in a complete switching cycle. The stages from  $t_0$ - $t_8$  are introduced and elaborated with the detailed corresponding equivalents circuits in Fig. 3 for every half-switching cycle.

**Stage 1 ( $t_0-t_1$ ):** As shown in Fig. 3(a), this mode starts ( $t = t_0$ ) when the gate pulses to switches  $S_2$ ,  $S_3$ , and  $S_6$  are removed and the freewheeling mode starts. The lossless snubbing capacitors  $C_{oss2}$ ,  $C_{oss3}$ , and  $C_{oss6}$  start getting charged by the resonant current  $i_s$ . The capacitor voltages  $V_{S2}$  and  $V_{S6}$  increase slowly from zero to  $V_{in}/2$  and  $V_{S3}$  to  $V_{in}$ . Alternatively, the body capacitors of switches  $S_1$ ,  $S_5$ , and  $S_4$  are discharged which results into a gradual decrease of their voltages from  $V_{in}/2$  and  $V_{in}$  to zero, respectively. The voltage across each resonant tank increases to  $V_{in}/2$ . The switches  $S_2$ ,  $S_3$ , and  $S_6$  turn-OFF with ZVS transition. This stage ends when the charging capacitors are fully charged and vice-versa.

**Stage 2 ( $t_1-t_2$ ):** As  $V_{S1}$ ,  $V_{S4}$ , and  $V_{S5}$  are equal to zero, the body capacitors are fully discharged. Mode 2 as depicted in Fig. 3(b) begins at this state. With the short-circuited switching state, the antiparallel diodes of switches start to conduct and become forward biased. Hence, the resonant tank power is fed back into the HVS with the negative resonant current flowing through  $D_{S1}$ ,  $D_{S4}$ , and  $D_{S5}$ . The secondary current runs into the load through  $Q_2$ ,  $Q_3$ , and  $Q_6$ . This stage ends when turn-ON signals are given to  $S_1$ ,  $S_4$ , and  $S_5$ .

**Stage 3 ( $t_2-t_3$ ):** As shown in Fig. 3(c), the triggering signals are provided to  $S_1$ ,  $S_4$ , and  $S_5$ , while  $D_{S1}$ ,  $D_{S4}$ , and  $D_{S5}$  are still conducting. The transformer current reaches zero at the end of this interval as the fed back power into the source

finishes. Moreover, the resonant current flows toward zero. Accordingly, ZVZCS turn-ON can be achieved for  $S_1$ ,  $S_4$ , and  $S_5$ . The output current becomes zero at the end of this stage.

**Stage 4 ( $t_3$ – $t_4$ ):** This mode is depicted in Fig. 3(d). The transformer current  $i_{oh1} = i_{oh2}$  reaches zero and starts to rise in a positive direction. The secondary current tries to flow in the negative direction; however, duty cycle control results in ZVS turn-ON of  $Q_3$  that short-circuits the transformer secondary with the body diode of already conducting  $Q_4$ . Hence, inhibiting the output current in reverse direction. Thus, there is no reverse power during this interval. In this mode, the current is discontinuous. This interval ends when  $Q_3$  is turned OFF. Moreover, the clamped zero voltage at  $L_m$  results in the constant magnetizing current ( $i_{Lm}$ ) in the transformer.

**Stage 5 ( $t_4$ – $t_5$ ):** The secondary current through the series connected windings of both the transformers starts to flow in the positive direction after  $Q_3$  and  $D_{Q4}$  are turned OFF. The positive current flows to load. On the HVS,  $S_1$ ,  $S_4$ , and  $S_5$  are conducting. On the secondary side, the body capacitors of  $Q_1$ ,  $Q_4$ , and  $Q_5$  discharge and  $Q_2$ ,  $Q_3$ , and  $Q_6$  are charged by the positive secondary current, which results in ZVS turn OFF. The positive voltage across secondary is reflected back to the HVS resulting in an increase in magnetizing current of both transformers toward the positive direction. The corresponding circuit is shown in Fig. 3(e).

**Stage 6 ( $t_5$ – $t_6$ ):** This interval begins when the body capacitors of  $C_{Q1}$ ,  $C_{Q4}$ , and  $C_{Q5}$  are discharged completely to zero voltage. The body diode  $D_{Q1}$ ,  $D_{Q4}$ , and  $D_{Q5}$  are conducting and remain in forward biased till the end of this interval when the trigger pulses are given as shown in Fig. 3(f). The secondary output current is positive during the interval.

**Stage 7 ( $t_6$ – $t_7$ ):** This stage starts with ZVS turn-ON of  $Q_1$ ,  $Q_4$ , and  $Q_5$ . The transient stage is depicted as Fig. 3(g). The forward power transfer from source to load takes place. The resonant current,  $i_{s1} = i_{s2}$ , goes toward positive through zero. The interval ends at the instant when  $i_{s1} = i_{s2}$  becomes zero. The current flows through switches instead of diodes.

**Stage 8 ( $t_7$ – $t_8$ ):** During this interval, the converter operates with positive power flow from HVS to LVS through the resonant tank and the transformers. This stage is represented by Fig. 3(h). The resonant waveforms change to a sine-waveform. Moreover, the magnetizing current  $i_{Lm}$  is increased through zero up to  $i_{Lm1}$ . The stage ends when  $S_1$ ,  $S_4$ , and  $S_5$  are turned OFF and are starting to go under dead-time operation.

### III. CHARACTERISTICS ANALYSIS

#### A. Fundamental Harmonic Analysis

The power is transmitted from input side to the output load side with the help of resonant tank components  $L_r$  (sum of  $L_{ext}$  and  $L_{lk}$ ),  $C_r$ ,  $L_m$ , and the phase shift ( $\varphi$ ) angle between the HV bridge and LV bridge. The current through the resonant components is nearly sinusoidal, as shown in Fig. 2. The approximate sinusoidal resonant current allows the FHA for dc analysis of the converter, which emphasizes that the fundamental component of any square wave is majorly responsible for power transfer

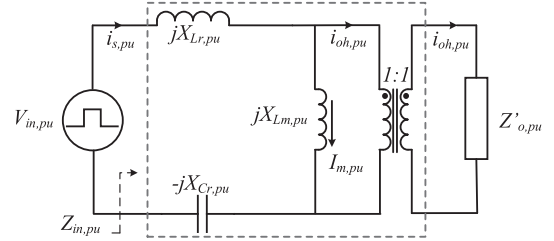


Fig. 4. Phasor domain equivalent two-port circuit of the proposed converter.

to the load. The ac-equivalent circuits for both resonant tanks are identical and given as an ac-equivalent two-port model, as shown in Fig. 4. All the switches, inductors, capacitors, and high-frequency transformers are ideal and lossless. Moreover, there is no effect of the snubber circuit and dead gap. The LV side parameters are transferred to the HV side and are denoted by a superscript ( $\cdot$ ). To begin with, all the parameters are normalized using following base quantities:

$$V_{base} = V_{in}, Z_{base} = \sqrt{\frac{L_r}{C_r}} = \omega_r L_r = \frac{1}{\omega_r C_r} \quad (1)$$

$$\omega_B = \omega_r = \frac{1}{\sqrt{L_r C_r}}, I_{base} = \frac{V_{base}}{Z_{base}} \quad (2)$$

where  $\omega_r = 2\pi f_r$  and  $f_r$  is the series resonant frequency.

The switching frequency in the normalized or per-unit form is defined as

$$F = \frac{\omega_s}{\omega_r} \quad (3)$$

where  $\omega_s = 2\pi f_s$  and  $f_s$  is the switching frequency.

With the objective to achieve ZVS/ZVZCS for primary as well as secondary switches, the converter is operated in the inductive region of gain curve, keeping  $f_s \geq f_r$ .

The per-unit reactance values in the resonant circuit are

$$X_{Lr,pu} = F, X_{Cr,pu} = \frac{1}{F}, X_{Lm,pu} = \frac{F}{k} \quad (4)$$

where  $k = L_r/L_m$  is the series-parallel inductance ratio in LLC resonant tank.

The per-unit fundamental input voltage on the primary side is given as

$$v_{in,pu}(t) = \sqrt{2}V_{in,rpu} \sin(\omega_s t) = \frac{4}{\pi} \sin(\omega_s t) \quad (5)$$

where  $V_{in,rpu} = \sqrt{8}/\pi$  is the per-unit fundamental rms voltage of  $v_{in}$ . The output voltage of the resonant tank at HF transformer is a quasi-square wave voltage whose fundamental value is

$$\begin{cases} v_{oh,pu}(t) = \sqrt{2}V_{oh,rpu} \cos\frac{\theta}{2} \sin(\omega_s t - \phi) \\ = \frac{4M}{\pi} \cos\frac{\theta}{2} \sin(\omega_s t - \phi) \end{cases} \quad (6)$$

where  $V_{oh,rpu} = \sqrt{8}M/\pi$  is the per-unit fundamental rms resonant tank output voltage,  $\phi$  is the controlled phase-shift angle between the input voltage and resonant tank output voltage,  $\theta$  is another controlled angle governed by the duty cycle control for secondary side switches, and  $M$  is converter voltage gain given

as

$$M = \frac{V'_{ol}}{V_{base}} = \frac{nV_{ol}}{V_{in}}. \quad (7)$$

The real output power is the average value of instantaneous power and per unit value is given as

$$P_{o,pu}(t) = \frac{8MF}{\pi^2(F^2 - 1)} \cos \frac{\theta}{2} \sin \phi. \quad (8)$$

As the range of  $\theta$  is  $[0, \pi/2]$ , the above equation reinforces the idea of positive/forward power flow for  $\phi \geq 0$  and backward power flow for  $\phi \leq 0$ .

Now the per-unit fundamental transformer current  $i_{oh,pu}(t)$  is

$$i_{oh,pu}(t) = \sqrt{2}I_{oh,rpu} \sin(\omega_s t - \beta) \quad (9)$$

where  $I_{oh,rpu}$  is the per-unit fundamental transformer rms current and  $\beta$  is the lagging phase angle with respect to  $v_{in,pu}(t)$ .

Using the analysis as in [33], the equivalent ac resistance  $R_{ac}$  must be replaced by modified equivalent ac impedance  $Z'_{o,M,pu}$ , which includes the secondary equivalent circuit referred to primary side consisting of active-rectifier. With the help of fundamental values of the transformer voltage and transformer current,  $\mathbf{Z}_{o,M,pu}$  can be calculated as the quotient. Using (6) and (9), it can be given as

$$\mathbf{Z}'_{o,M,pu} = \frac{\sqrt{2}V_{oh,rpu} \cos \frac{\theta}{2} \sin(\omega_s t - \phi)}{\sqrt{2}I_{oh,rpu} \sin(\omega_s t - \beta)} = \frac{\cos^3 \frac{\theta}{2}}{Q} \angle(-\theta) \quad (10)$$

where  $\theta = \phi - \beta$  is the phase angle of the modified ac equivalent impedance and the quality factor  $Q$  is given as

$$Q = \frac{\pi^2 Z_{base} P_o}{8n^2 V_o^2}. \quad (11)$$

The phase angle  $\theta$  and  $\beta$  has a direct relationship with the controlled phase-shift angle  $\phi_{as}$

$$\begin{aligned} \theta &= \arctan \left[ \frac{M}{\sin \phi} (1 + k - k/F^2) - \cot \phi \right] \\ \beta &= \arctan \left[ \frac{\sin \phi}{M (1 + k - k/F^2)} - \cot \phi \right]. \end{aligned} \quad (12)$$

While observing the phasor-domain equivalent circuit, the input impedance can be defined as

$$\mathbf{Z}_{in,pu} = j(F - \frac{1}{F}) + \mathbf{Z}'_{o,M,pu} \parallel j \frac{F}{k} = |\mathbf{Z}_{in,pu}| \angle \alpha \quad (13)$$

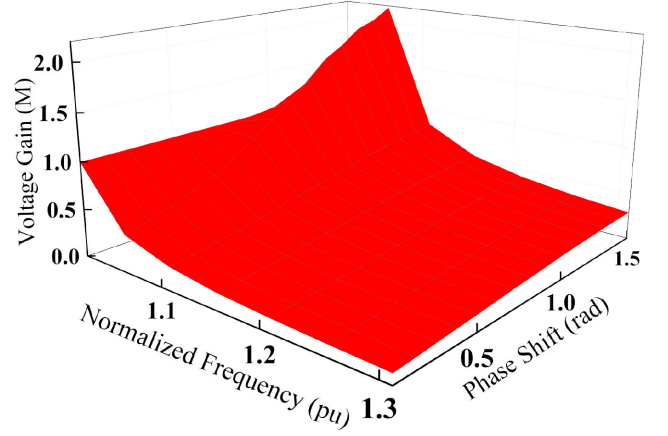


Fig. 5. Plot of voltage gain with respect to normalized switching frequency and phase shift for  $k = 0.65$  and  $Q = 2$ .

where

$$\begin{aligned} |Z_{in,pu}| &= \frac{Z_1 + jZ_2}{Z_3} Z_1 = \frac{F}{k}, \\ Z_2 &= \left[ \left(F - \frac{1}{F}\right) \left( \frac{k \cos^3 \theta / 2}{FQ \cos \theta} + \frac{FQ}{k \cos \theta \cos^3 \theta / 2} - 2 \tan \theta \right) \right. \\ &\quad \left. + \frac{\cos^3 \theta / 2}{Q \cos \theta} - \frac{F}{k} \tan \theta \right] \\ Z_3 &= \frac{k \cos^3 \theta / 2}{FQ \cos \theta} + \frac{FQ}{k \cos \theta \cos^3 \theta / 2} - 2 \tan \theta \end{aligned} \quad (14)$$

where

$$\begin{aligned} \alpha &= \arctan \left( \frac{Z_2}{Z_1} \right) = \arctan \left[ \left(F - \frac{1}{F}\right) \left( \frac{k^2 \cos^3 \theta / 2}{F^2 Q \cos \theta} \right) \right. \\ &\quad \left. + \frac{Q}{\cos \theta \cos^3 \theta / 2} - \frac{2k}{F} \tan \theta \right] + \frac{k \cos^3 \theta / 2}{FQ \cos \theta} - \tan \theta \end{aligned} \quad (15)$$

## B. Voltage Gain

As the converter operates in the inductive region, the operating frequency is always greater than the resonant frequency. The voltage gain of the proposed converter can be calculated by analyzing the two-port model, and is given as

The simplified equation of the voltage gain is given as (17), as shown at the bottom of this page. The voltage gain is plotted against the normalized switching frequency, as shown in Fig. 5. It can be observed that the converter voltage gain is varied broadly for all phase-shift values making it employable for wide input voltage range. The narrow frequency variation to keep voltage

$$M = \left| \frac{\mathbf{V}_{oh,pu}}{\mathbf{V}_{in,pu}} \right| = \left| \frac{\mathbf{Z}'_{o,M,pu} \parallel jF/k}{\mathbf{Z}_{in,pu}} \right| \quad (16)$$

$$M = \sqrt{\frac{\left(\frac{F}{k}\right)^2 + \left(\frac{\cos^3 \theta / 2}{Q \cos \theta} - \frac{F}{k} \tan \theta\right)^2}{\left(\frac{F}{k}\right)^2 + \left[\left(\frac{\cos^3 \theta / 2}{Q \cos \theta} - \frac{F}{k} \tan \theta\right) + \left(F - \frac{1}{F}\right) \left(\frac{k \cos^3 \theta / 2}{FQ \cos \theta} + \frac{FQ}{k \cos^3 \theta / 2} - 2 \tan \theta\right)\right]^2}} \quad (17)$$

TABLE I  
VOLTAGE AND CURRENT STRESS SUMMARIZED

Power Semiconductor switches	Voltage Stress	Current Stress
$S_1/S_2/S_5/S_6$	$\frac{V_{in}}{2}$	$\frac{2F}{\pi(F^2-1)} \sqrt{1 + M^2 \cos^2 \frac{\theta}{2} - 2M \cos \phi \cos \theta/2}$
$S_3/S_4$	$V_{in}$	
$Q_1/Q_2/Q_5/Q_6$	$\frac{V_0}{2}$	$\frac{2nF}{\pi(F^2-1)} \sqrt{1 + M^2 \cos^2 \frac{\theta}{2} - 2M \cos \phi \cos \theta/2} - \frac{2nM}{\pi F} k \cos \frac{\theta}{2}$
$Q_3/Q_4$	$V_0$	

gain constant is the added advantage of the employed modulation scheme.

### C. Voltage and Current Stresses of Power Switches

Based on the operation principles as discussed above, the peak voltage stresses on  $S_1 \sim S_6$  (except  $S_3/S_4$ ) are  $V_{in}/2$  and  $S_3/S_4$  are  $V_{in}$ . The peak voltage stresses on  $Q_1 \sim Q_6$  (except  $Q_3/Q_4$ ) are  $V_0/2$  and  $Q_3/Q_4$  are  $V_0$ . The peak current stresses are summarized in Table I.

### D. Soft Switching Analysis

1) *ZVS in Primary MOSFETs*: The soft switching achievement of the power MOSFETs plays an important role to ascertain that the converter operates in high conversion efficiency. However, the necessary constraint for the primary MOSFETs is the resonant current being inductive with reference to the fundamental primary input voltage. This relation in analytical form can be written as  $\alpha > 0$ .

Using (15) and simplifying, we have

$$\tan^{-1} \left[ \left( F - \frac{1}{F} \right) \left( \frac{k^2 \cos^3 \theta/2}{F^2 Q \cos \theta} + \frac{Q}{\cos \theta \cos^3 \theta/2} - \frac{2k}{F} \tan \theta \right) + \frac{k \cos^3 \theta/2}{F Q \cos \theta} - \tan \theta \right] \geq 0. \quad (18)$$

After the simplification of (18), using (12), we have

$$F - \frac{1}{F} \geq \frac{\sin 2\phi - \cos^3 \theta/2}{3Q}. \quad (19)$$

For any values of  $\phi$  and  $\theta$ ,  $\sin 2\phi - \cos^3 \theta/2$  will always be less than unity, thus further simplifying (19) to

$$F - \frac{1}{F} \geq \frac{1}{3Q}. \quad (20)$$

The above equation defines the switching frequency range for any selected Q-value for the desired ZVS in all primary MOSFETs. The variation of the input impedance angle ( $\alpha$ ) with respect to phase-shift angle and the converter gain for a range of Q-values have been plotted in Fig. 6 using (15). It can be seen that the apt selection of phase shift for power transfer can achieve the ZVS in primary switches for the complete range of Q-values for the selected range of switching frequency. Hence, the positive  $\alpha$  for M greater than unity under all Q-values demonstrates the ZVS achievement also for light-load condition, which is usually lost

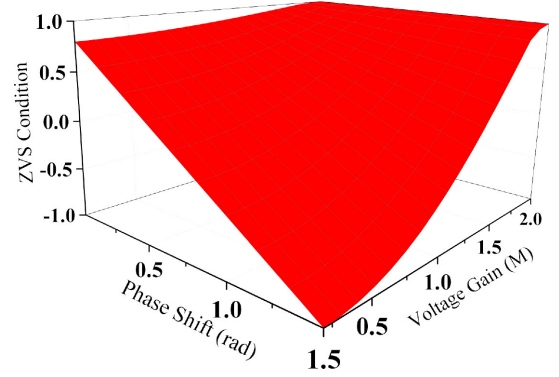


Fig. 6. Plot of  $\alpha$  versus  $\phi$  and M at  $F = 1.1$  and  $k = 0.65$  for ZVS Condition in primary switches.

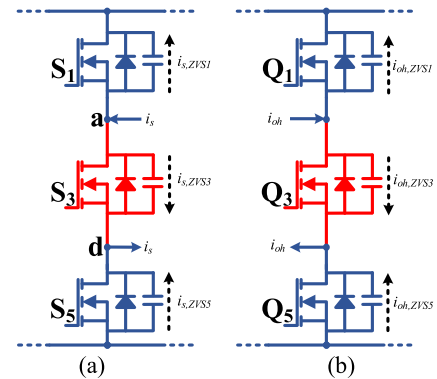


Fig. 7. Resonant current direction. (a) Primary switches. (b) Secondary switches.

when conventional PSM is used. This implies the wider range of ZVS for all primary MOSFETs.

However, as per the dynamics of the converter, the instantaneous resonant current must be large enough to discharge or charge the lossless snubbing capacitances of the MOSFET for turn-ON and turn-OFF switching operation, respectively. The resonant current for the primary and secondary switches in one-leg of the bridges have been shown in Fig. 7. The resonant current  $i_s$  on the primary side is negative. However, the absolute value of  $i_s$  should be larger than the resonant current  $I_{s,ZVS}$  consisting of the resonant tank and the output capacitance of the respective MOSFET during switching transient. The discharging resonant current for MOSFET  $S_1$  and  $S_5$  would be equal and given as  $I_{s,ZVS1}$ , while the charging current for  $S_3$  is given as  $I_{s,ZVS3}$

with switch voltage different from  $S_1$  and  $S_5$

$$I_{s,ZVS1} = \frac{C_{oss\_S} \cdot V_{in}/2}{T_d}, I_{s,ZVS3} = \frac{C_{oss\_S} \cdot V_{in}}{T_d}. \quad (21)$$

As discussed above, the sufficient condition for ZVS in the primary switches is  $\sqrt{2}I_{s,r} \sin \alpha \geq I_{s,ZVS1}$ , and by using (21), it can be written as

$$\tan \alpha \geq \frac{C_{oss\_S} \cdot V_{in}^2}{2\pi P_{in} T_d} \quad (22)$$

$$\Rightarrow ZVS_p(\phi, \theta) = \cot \phi - \frac{1}{M \sin \phi \cos \theta/2} \geq \frac{C_{oss\_S} \cdot V_{in}^2}{2\pi P_{in} T_d} \quad (23)$$

where  $C_{oss\_S}$  is the output capacitance of primary MOSFETs and  $T_d$  is the gating signal deadband.

2) *ZVS in Secondary MOSFETs*: On a similar note as in primary switches, the ZVS in secondary MOSFETs can be achieved by calculating the phase angle between transformer current and voltage. The capacitive transformer current with reference to quasi-square transformer voltage makes sure that the ZVS has been secured. Hence, to sustain the ZVS in the secondary side, the necessary condition is  $\phi - \beta = \theta \geq 0$ . Using (12), the same can be written as

$$\left[ \frac{M}{\sin \phi} (1 + k - k/F^2) - \cot \phi \right] > 0$$

$$\Rightarrow M > \frac{\cos \phi}{1 + k - k/F^2}. \quad (24)$$

The above equation defines the necessary requirement for ZVS in the secondary switches for all values of phase shift,  $\phi$ .

As in primary switches, the secondary MOSFET body diode must be conducted before its turn ON. The positive transformer current,  $i_{oh}$  going into the MOSFET, as shown in Fig. 7(b) should be large enough to charge and discharge the body capacitance of the secondary MOSFETs during the switching operation. The absolute value of  $i_{oh}$  should be higher than the resonant current,  $I_{oh,ZVS}$  consisting of the input resonant tank and the output capacitance of the secondary MOSFETs during switching transient. The discharging resonant current for MOSFET  $Q_1$  and  $Q_5$  would be equal and given as  $I_{oh,ZVS1}$ , while the charging current for  $Q_3$  is given as  $I_{oh,ZVS3}$  with switch voltage different from  $S_1$  and  $S_5$

$$I_{oh,ZVS1} = \frac{C_{oss'_S} \cdot V_{in}/2}{T_d}, I_{oh,ZVS3} = \frac{C_{oss'_S} \cdot V_{in}}{T_d}. \quad (25)$$

As discussed above and using (9), we have

$$i_{oh,pu}(-90 - \phi)$$

$$= \frac{4F}{\pi(F^2 - 1)} (-\sin \phi + M \cos(\theta/2) \sin(2\phi))$$

$$+ \frac{4F}{\pi k} M \cos \theta/2 \sin(2\phi) \geq 0 \quad (26)$$

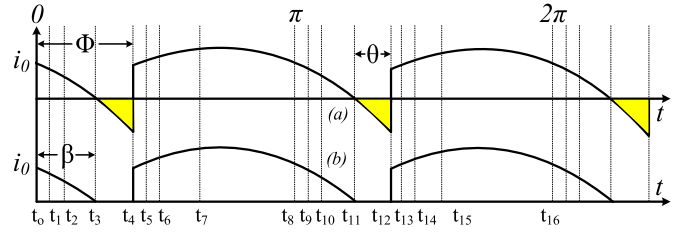


Fig. 8. Comparison of output current. (a) SPS modulation. (b) Proposed modulation.

$$\Rightarrow ZVS_s(\phi, \theta) = k \leq \frac{(F^2 - 1) [M \cos(\theta/2) \sin(2\phi)]}{\sin \phi - M \cos(\theta/2) \sin(2\phi)}. \quad (27)$$

The inductor ratio  $k$  can be selected for the required range of ZVS in the secondary switches. The switching frequency variation with reference to load Q-values has been defined in (20) for the soft switching operation of the primary MOSFETs. Henceforth, ZVS can be realized for all MOSFETs whenever the operation of the converter is within the ZVS conditions as defined in the above discussion.

#### E. Reverse Power Flow

When the power flows from input to output, a part of power freewheels back to input side due to the phase difference between the transformer voltage and current. This reverse power flow causes an increase in conduction losses due to freewheeling energy. This becomes severe under minimum input voltage and light-load conditions causing severe conduction losses and thereby affecting the performance of the converter. The operating waveforms for the output current under SPS modulation and the proposed modulation have been drawn in Fig. 8. The shaded yellow portion corresponds to the reverse power from output side to input side. The negative output current during  $t_3$ – $t_4$  duration causes the reverse power flow in the converter. The reverse power in a half cycle is given as:

$$P_r = \frac{1}{\pi} \int_{0.5 - \frac{\theta}{\pi}}^{\pi} v_{oh}(\omega_s t) \cdot i_o(\omega_s t) d(\omega_s t). \quad (28)$$

For the proposed modulation, the duty ratio control limits the output current from going negative and remain zero for the desired time interval. Hence,  $i_o(\omega_s t) = 0$  for  $(t_3$ – $t_4)$  interval.

Hence, the reverse power is zero in the proposed converter which can be verified through operating waveforms as in Fig. 3. The theoretical as well as experimental duty ratio value for the desired switches have been summarized in Table III.

#### IV. DESIGN CONSIDERATIONS AND PARAMETER SELECTIONS

On the note of detailed steady-state analysis, a design sample of the prototype is provided in the section. The converter parameters are selected as per the required objectives. The prototype to be built has the following design specifications.

- 1) Power rating,  $P_o = 1.5$  kW.
- 2) Input voltage range,  $V_{in} = 210$ – $400$  V.

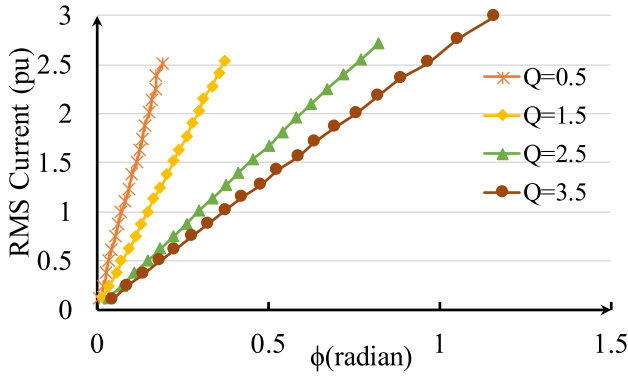


Fig. 9. Plot of per unit rms resonant current ( $I_{S,RMS,pu}$ ) versus  $\phi$  at different  $Q$  values for  $F = 1.1$  and  $k = 0.65$ .

### 3) Output Voltage, $V_o = 80$ V.

The significance of the design objectives is to maintain high and wide input voltage range, achieve ZVS operation for the entire load range, and eliminate the RPF due to circulating current at all load conditions. The converter gain in (17) defines its relationship with the phase-shift angle and duty cycle control. The ZVS conditions given in (23) and (27) are sufficient but hard to analyze pertaining to dependence on the output capacitance and the circuit operation. Hence, the conditions in (20) and (24) are utilized for ZVS realization in designing.

#### A. Selection of Quality Factor, $Q$

The quality factor  $Q$ , having other parameters fixed, must be selected to reduce the size of the reactive components and to have minimum resonant rms current. The quality factor is directly proportional to  $L_r$ ,  $L_m$ , and inversely to  $C_r$  as seen in (1)–(9). Hence, to have smaller inductive and magnetic components,  $Q$ -value should be small. However, smaller  $Q$ -value, using (20), could result in larger switching frequency range making it complex for magnetic components optimization. Moreover, smaller  $L_m$  could cause larger magnetizing current independent of load flowing through the parallel inductor. The plot in Fig. 9 illustrates the variation of resonant rms current with respect to phase shift for different  $Q$ -values at fixed  $M$ ,  $F$ , and  $k$  value. From the plot, it can be concluded that the rms current reduces for smaller  $Q$  values although insignificantly. After the above considerations, a tradeoff has to be made, and full load  $Q$  value equal to 2.8 is chosen.

#### B. Selection of Normalized Switching Frequency Range, $F$

The switching frequency range plays a vital role in the proper selection of magnetic components. It also ensures ZVS operations in all MOSFETs on primary as well as on secondary bridges. For the selected  $Q = 2.8$  value, the switching frequency range can be calculated using (20). The sequential frequency selection with varying load results in load independent voltage gain. For the desired operation of load change from 20% load to full load, the quality factor  $Q$  ranges from 0.56–2.8, respectively. This range of  $Q$  value results in the normalized switching frequency range of 1.061–1.341, which is calculated using (20). This range

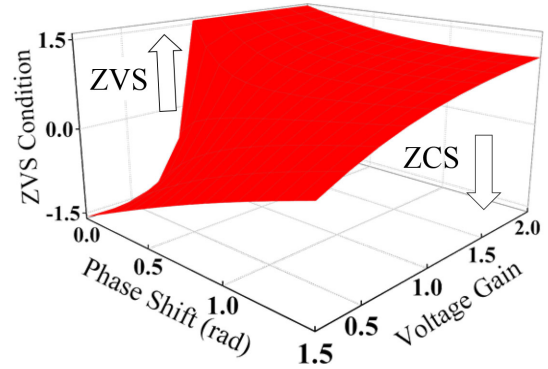


Fig. 10. Plot of  $\theta$  versus  $\phi$  and  $M$  at  $F = 1.1$  and  $k = 0.65$  for ZVS condition in secondary switches.

can be iteratively attuned to keep ZVS check and enhance converter performance.

#### C. Converter Gain Selection, $M$

The converter gain,  $M$  should be chosen in such a manner that the ZVS conditions are maintained for all input voltage and load variations. In order to select the minimum converter gain  $M_{min}$ , the plot of  $\theta$  versus  $\phi$  for different  $M$  value has been analyzed, as in Fig. 10. For any selected value of converter gain  $M$  greater than 0.84, the ZVS conditions are satisfied. From the above discussion, we have

$$M_{min} = 0.84.$$

Therefore, with the design point of maximum input voltage, the transformer turn ratio can be calculated as

$$n = \frac{M_{min} \cdot V_{in\_max}}{V_o} \quad (29)$$

$$n = 21 : 5. \quad (30)$$

Using  $n$ , the maximum converter gain is calculated as

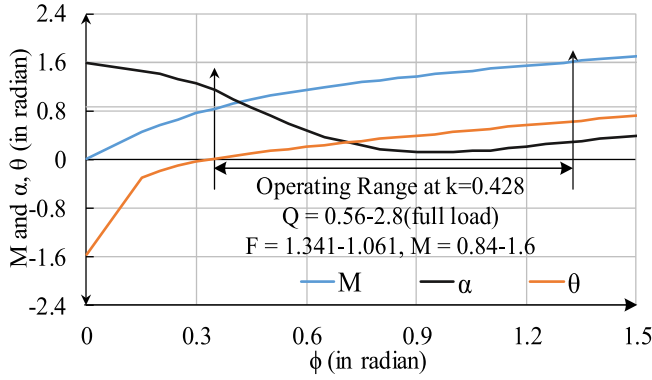
$$M_{max} = \frac{n \cdot V_o}{V_{in\_min}}. \quad (31)$$

Hence

$$M_{max} = 1.6. \quad (32)$$

#### D. Selection of Inductor Ratio, $k$

The inductor ratio  $k$  does not affect the voltage gain values in the proposed converter. The inductor ratio  $k$  (or magnetizing inductor  $L_m$ ) governs the ZVS range of secondary MOSFET switches. The larger the inductor ratio  $k$  is, the larger is the ZVS range. However, the conventional PSM and variable frequency PSM proposed in [14] discuss the limitation of larger inductor ratio  $k$  of having increased reactive power in the converter under light-load conditions. The circulating current causes increased conduction losses thereby reducing the converter efficiency. However, this limitation can be overcome using the proposed modulation scheme.

Fig. 11. Plot of gain (M),  $\alpha$ , and  $\theta$  versus  $\phi$  at the operating conditions.TABLE II  
DESIGNED SPECIFICATIONS OF THE PROTOTYPE

Parameters	Value
Rated Output Power, $P_o$	1500 W
Input Voltage, $V_{in}$	210-400 V
Output Voltage, $V_o$	80
Resonant Frequency, $f_r$	75 kHz
Transformer Turns ratio (n:1)	4.2
Resonant Inductor ( $L_{r1}$ , $L_{r2}$ )	181.26 $\mu$ H
Resonant Capacitors ( $C_{r1}$ , $C_{r2}$ )	24.82 nF
Output Filter Capacitor ( $C_o$ )	100 $\mu$ F
Magnetizing Inductance ( $L_{m1}$ , $L_{m2}$ )	423.5 $\mu$ H
Load Resistance, $R_o$	4.27 $\Omega$

Based on the discussion, the ZVS condition in (24) should be satisfied by the selected inductor ratio  $k$ . Thereby calculating inductor ratio  $k$  at the extreme conditions, i.e.,  $\phi = 0$ , no-load,  $F_{max} = 1.341$ ,  $M_{min} = 0.84$ , yields

$$k > 0.428. \quad (33)$$

With  $k = 0.428$ , the variation of  $M$ ,  $\alpha$ , and  $\theta$  with respect to phase shift has been plotted in Fig. 11 for selected values of  $Q$  and  $F$ . It can be established that  $\alpha$  and  $\theta$  are always positive in the entire range of operation. In other words, ZVS is achieved for both primary as well as secondary MOSFETs for the selected gain range of 0.84–1.6.

Finally, using (1)–(4), and (11), the resonant components has been calculated as discussed further

$$L_r = \frac{8R_o Q n^2}{\pi^2 \omega_r} = 362.52 \mu\text{H} \quad (34)$$

$$C_r = \frac{\pi^2}{8\omega_r R_o Q n^2} = 12.41 \text{ nF} \quad (35)$$

$$L_m = \frac{L_r}{k} = 847 \mu\text{H}. \quad (36)$$

With the calculated resonant tank components, the complete design specifications of the converter are given as in Table II.

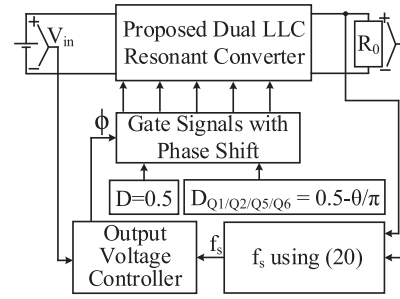


Fig. 12. Block diagram of the proposed modulation scheme.

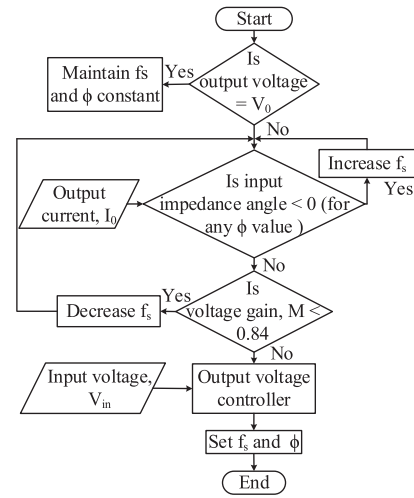


Fig. 13. Flowchart for the proposed control scheme.

## V. CONTROL SCHEME

As seen in (8), the power transferred to the output is controlled by phase shift angle ( $\phi$ ) along with the switching frequency ( $f_s$ ) and the control angle  $\theta$  (defining the duty ratio for secondary switches). A simplified block diagram of the proposed technique has been shown in Fig. 12.

The switching frequency range is defined solely by the variation of load,  $Q$ -values to achieve ZVS in the primary MOSFETs. The selective frequency approach minimized the effect of  $Q$ -value and maintained an identical voltage gain characteristic of all phase-shift angle values. Furthermore, the phase-shift angle is regulated to maintain the constant output voltage for varying input voltage and maintain the frequency range within the defined limits. Additionally, the duty ratio control of the secondary switches ( $Q_1/Q_2$  and  $Q_5/Q_6$ ) calculates the suitable duty ratio to eliminate the reverse power in the converter. In order to implement the derived control law, a high precision DSP TMS320F28335 with system clock of 150 MHz is employed. The ePWM module operating in up and down count mode generates the gate signals for the switches. The A/D input of the DSP samples the voltage input and regulate the phase shift, switching frequency, and duty ratio by changing the register values. Hence, the output voltage can be maintained for required values using the control flowchart as shown in Fig. 13.

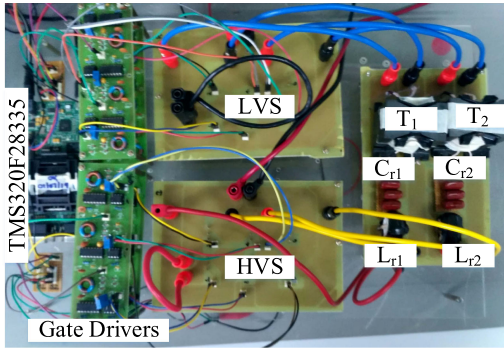


Fig. 14. Lab-built prototype of the proposed converter.

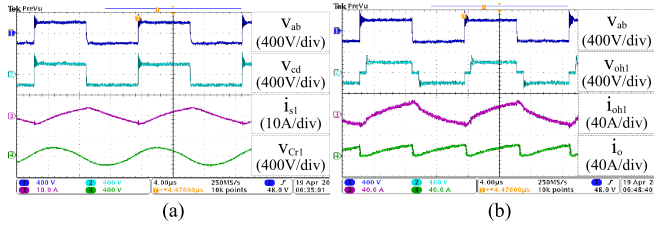


Fig. 15. Steady-state waveforms of the converter at full-rated load for  $V_{in} = 400$  V and  $V_o = 80$  V.

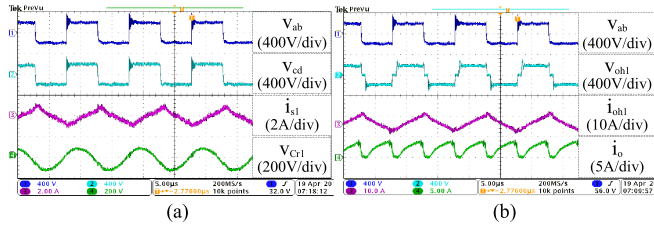


Fig. 16. Steady-state waveforms of the converter at 20% load for  $V_{in} = 400$  V and  $V_o = 80$  V.

## VI. EXPERIMENTAL RESULTS

A 1.5-kW lab prototype of the proposed dual LLC resonant dc–dc converter with the resistive load was built and effectively tested to verify the theoretical as well as simulation results, which is illustrated in Fig. 14. The parameters and specifications of the converter have been listed in Table II. The input voltage varies from 210–400 V maintaining a constant 80-V output voltage. To achieve reduced power losses and for high-frequency operation, SiC MOSFETs C2M0280120D are used as  $S_1 \sim S_6$  suitably rated for medium to high voltage applications. IRFSL4227PbF have been chosen as secondary MOSFETs. It is noteworthy that the primary MOSFET's peak voltage stress of the proposed circuit is 200 V for four out of six MOSFETs. However, due to the availability of the switching devices in laboratory, 1200-V SiC MOSFETs are used in the prototype design. The deadband is sufficiently chosen so achieve the ZVS operation. The multithread Litz wire is used for the windings with transformer turns ratio 21:5. Hence, the magnetizing inductance of each transformer is 423.5  $\mu$ H.

The experimental waveforms for forward power flow operation depicting the similar characteristics as in are presented in Figs. 15–18. The operating switching frequency varies with

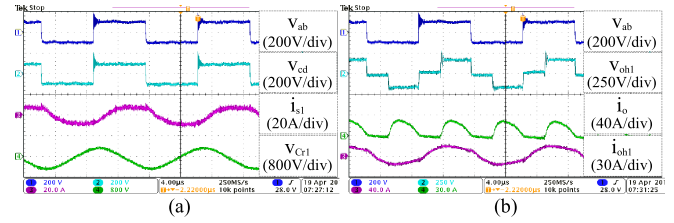


Fig. 17. Steady-state waveforms of the converter at full-rated load for  $V_{in} = 210$  V and  $V_o = 80$  V.

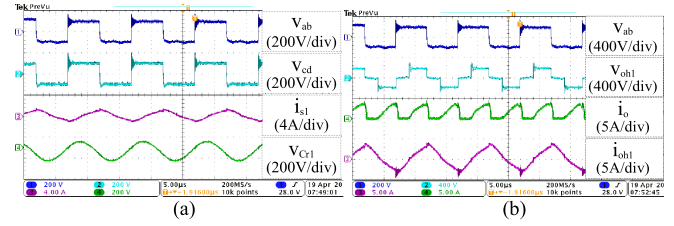


Fig. 18. Steady-state waveforms of the converter at 20% load for  $V_{in} = 210$  V and  $V_o = 80$  V.

the load only and remains fixed for constant load irrespective of input voltage values. For changing input voltages,  $\phi$  changes to regulate the output voltage constant regardless of changing loading conditions. It is observed that for low input voltages, the duty ratio of  $S_3/S_4$  reduces largely to compensate for the increased reverse power. Henceforth, for the identical power output, the current  $i_o$  shows larger zero current portion at 210 V than 400 V, which can be verified in the subsequent results.

Fig. 15 shows the key waveforms in forward power flow operation of the converter at 400-V input voltage under full load condition. Fig. 15(a) depicts the identical square voltage from the primary LV bridge. The resonant capacitor voltage,  $v_{cr}$  is nearly sinusoidal as can be seen from the waveform. Fig. 15(b) shows the experimental waveforms for the square input voltage, quasi-square transformer primary voltage, the secondary current, and the output current. It can be seen in Fig. 15(b), the circulating current could exist if there is no duty cycle control of the secondary upper and lower leg switches. However, there is no circulating current (eliminated negative current portion) in the output side of the converter.

Fig. 16 shows the key waveforms for the forward power flow operation under 20% load condition at 400-V input voltage. The larger amount of circulating current under light-load condition needs larger duty cycle control, which can be observed in the output side current waveform in Fig. 16(b), thereby eliminating the circulating current. The primary resonant current waveform is quite similar to theoretical resonant current. Figs. 17 and 18 show the keys waveforms for the forward power flow under 210-V input voltage for full load and 20% load conditions, respectively.

Figs. 19 and 20 illustrate the ZVS operation of the primary switches under different loading conditions at maximum and minimum input voltage. Fig. 19 shows the gate signal and drain-source voltage ( $V_{ds}$ ) waveforms of switches  $S_1$ ,  $S_3$ , and  $S_5$  at maximum input voltage under different load condition. The  $V_{ds}$  goes zero before the gate turn-ON of the switch signifies the ZVS

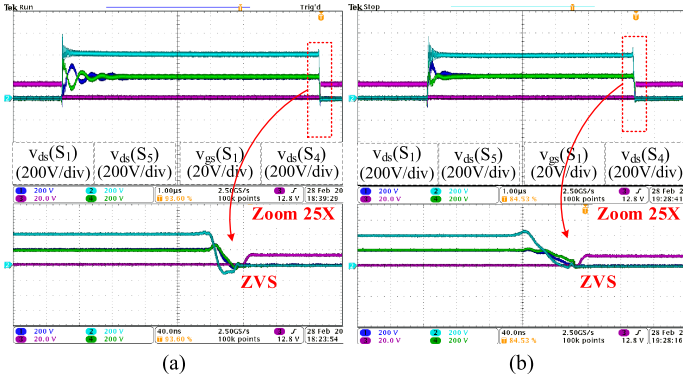


Fig. 19. Experimental waveforms of the primary MOSFETs for  $V_{in} = 400$  V. (a) Full load. (b) 20% load.

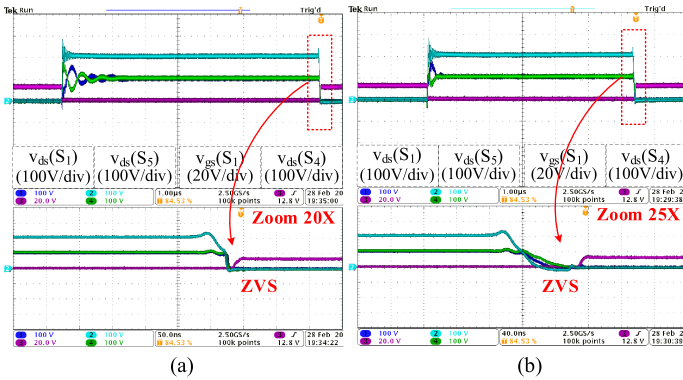


Fig. 20. Experimental waveforms of the primary MOSFETs for  $V_{in} = 210$  V. (a) Full load. (b) 20% load.

operation of the switches. As ZVS is illustrated on both sides during turn-ON, the turn-ON switching losses become insignificant. It is noteworthy that there is switching instant drain-source voltage mismatch between the series-connected switches for which external circuitry would be required to balance the voltage for transient as well as steady-state condition [34]. However, the added auxiliary circuit for the switches would result in increased cost and size of the driving circuits. The same can be verified from Figs. 19 and 20. Figs. 21–24 present the ZVS turn-ON of the secondary switches. The  $V_{ds}$  waveform does not depict any significant voltage spikes across the switch, which implies the ZVS turn-ON operation. The experimental waveforms verify the ZVS operation of the secondary MOSFETs for different load and input condition.

Fig. 25 shows the overall efficiency curve of the proposed dual-phase LLC resonant converter at maximum and minimum input voltage. As can be observed, the proposed converter operated at high efficiency for the wide input and load range conditions. Moreover, for the peak input voltage, the efficiency variation is narrow over the entire load range.

The power loss distribution and comparison of the proposed converter and the conventional FB LLC [35] has been done and presented in Fig. 26. The power loss analysis is conducted with mathematical formulas proposed in [36]. The loss breakdown

TABLE III  
PARAMETERS FOR DIFFERENT INPUT AND LOAD CONDITIONS

$V_{in}$	Q	$F_s$	$\Phi$	$\theta$	D ( $Q_1/Q_2/Q_3/Q_4$ )
400V	Full load Q=2.8	F=1.061	Th	18.9°	5.33
			Ex	19.8°	6.36°
400V	20% load Q=0.56	F=1.341	Th	18.9°	8.9°
			Ex	19.8°	9.2°
210V	Full load Q=2.8	F=1.061	Th	77°	35.52°
			Ex	79°	36.9°
210V	20% load Q=0.56	F=1.341	Th	77°	35.86°
			Ex	79°	37.15°

has been done at full load condition and 400-V input. As shown, the distribution comprises of primary MOSFET losses, secondary MOSFET losses, transformer core loss, transformer conduction loss, inductor conduction loss, and other losses. The primary as well as secondary MOSFET losses are less than the conventional FB losses owing to ZVS, and the turn-OFF transition switching losses are reduced to a very small value. The extra losses in conventional FB LLC occur due to nonfull ZVS characteristics. The transformer core losses depend upon the volume of the transformer core. The higher transformer conduction losses occur pertaining to higher number of winding turns. To validate the steady-state analysis, all the important angles, switching frequency values, and duty ratios for different input and load values have been summarized in Table III.

## VII. PERFORMANCE COMPARISON

An overview comparison of the resonant converters has been summarized in Table IV. Moreover, the parameter and component comparison of the proposed topology has been done with conventional FB LLC [35] and an improved FB LLC [37] in the Table V. The detailed parameters of the three converters have been summarized in the table following the design procedure as discussed in [33]. As seen, the resonant capacitor in the proposed topology is larger than the others; however, its peak voltage as calculated for the same values of resonant current is much smaller. This results in smaller volume of resonant capacitor. Second, although the primary bridge has been modified, the ZVS range of conventional LLC DAB is well preserved and extended using the improved modulation scheme. For transformer sizing, the comparison of area product and volume can be done for the three converters. Moreover, the component counts of the proposed converter are more than conventional FB LLC and lesser than the improved FB LLC. However, the voltage stress comparison on the switches of the three topologies results in cost comparison based on topology configuration. To further, highlight the merits of the proposed topology, a cost comparison has been considered and presented in Table VI. For the cost comparison, identical voltage parameters have been used for all topologies. From the resultant cost given in Table VI, the proposed topology gives the minimum cost for the switch compared to other topologies.

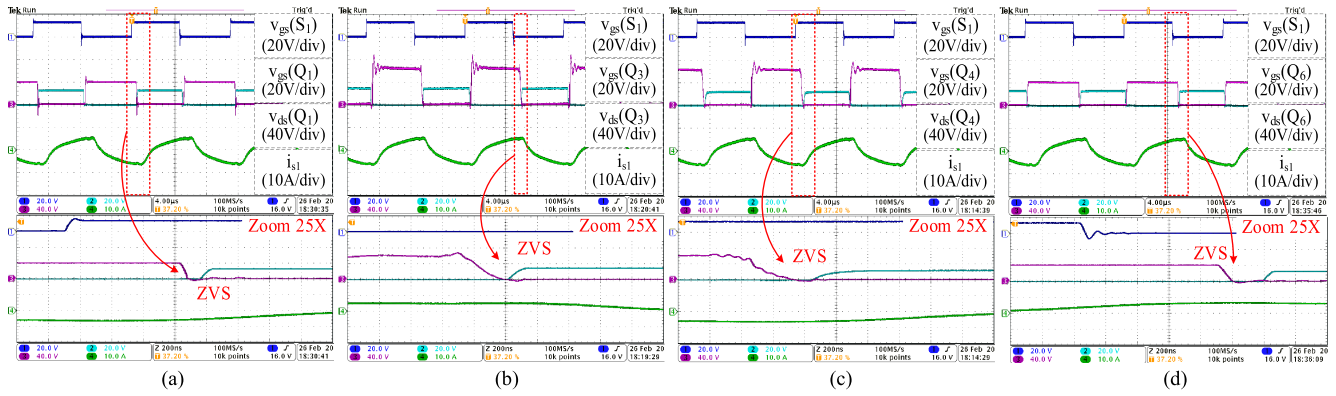


Fig. 21. Experimental waveforms of the secondary MOSFETs at full load for  $V_{in} = 400$  V and  $V_o = 80$  V. (a) Q1. (b) Q3. (c) Q4. (d) Q6.

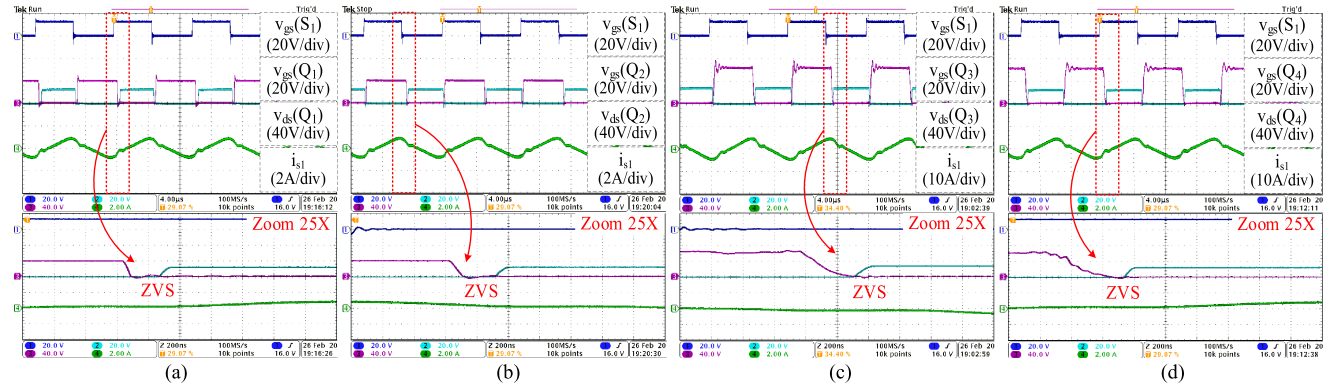


Fig. 22. Experimental waveforms of the secondary MOSFETs at 20% load for  $V_{in} = 400$  V and  $V_o = 80$  V. (a) Q1. (b) Q2. (c) Q3. (d) Q4.

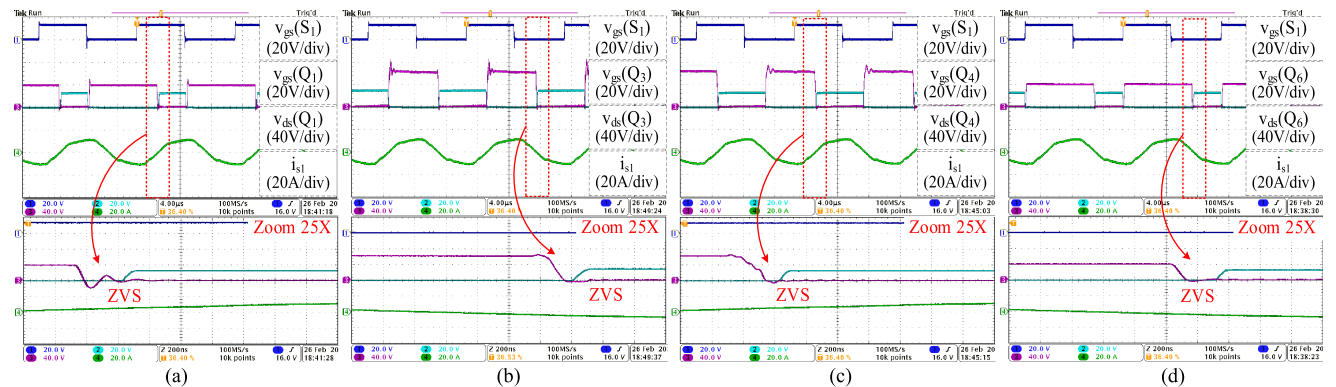


Fig. 23. Experimental waveforms of the secondary MOSFETs at full load for  $V_{in} = 210$  V and  $V_o = 80$  V. (a) Q1. (b) Q3. (c) Q4. (d) Q6.

TABLE IV  
OVERVIEW COMPARISON OF THE PROPOSED CONVERTER WITH OTHER RECENT TOPOLOGIES

Topologies	[14]	[15]	[20]	[38]	[39]	Proposed Converter
MOSFETs	6	12	10	8	5	12
Diodes	0	0	0	0	4	0
Number of Transformers	1	1	1	2	2	2
Capacitors	3	4	1	1	3	1
Modulation	FAPSM	PWAM	DPS	PFM	PFM	VF-PSM
Gain range (with load)	Wide/Independent	Wide	Narrow/Dependent	Medium/dependent	Wide	Wide/Independent
ZVS performance	Excellent	Medium	Good	Good	Excellent	Excellent
Reverse power Flow	Yes	Yes	No	Yes	Yes	No
Input	200-400	240-480 V	60 V	330-410 V	390V	210-400 V
Output	48V/ 1kW	30-60V/ 1kW	13.5 V/ 350W	14 V/ 2.5 kW	80-450V/ 1kW	80 V/ 1.5kW
Peak efficiency	96.4%	96.5%	96.3%	95%	97.01%	96.7%

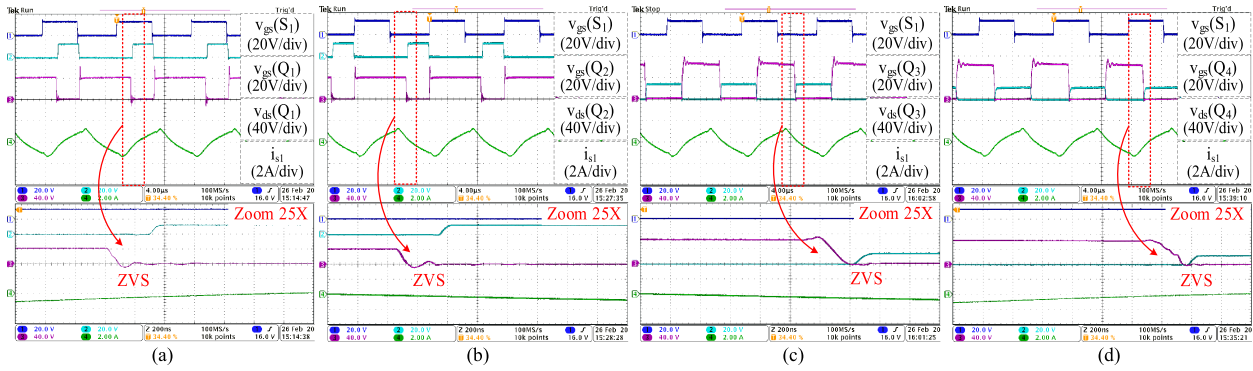


Fig. 24. Experimental waveforms of the secondary MOSFETs at 20% load for  $V_{in} = 210$  V and  $V_o = 80$  V. (a)  $Q_1$ . (b)  $Q_2$ . (c)  $Q_3$ . (d)  $Q_4$ .

TABLE V  
COMPONENTS AND PARAMETERS COMPARISON OF THE PROPOSED CONVERTERS

Parameters or Components	Conventional FB LLC [35]	Improved FB LLC [37]	Proposed Converter
Turn-ratio $n_s, n_1, n_2$	4.2, -, -	4.2, 3, 1.2	4.2, 2.1, 2.1
Inductance ratio $k$	0.586	0.323 ( $L_r/L_m$ ), 0.465 ( $L_r/L_{m1}$ )	0.428
Resonant Inductance $L_{r1}, L_{r2}$	827.49 $\mu$ H, n/a, n/a	710.6 $\mu$ H, n/a, n/a	362.52 $\mu$ H, 181.26 $\mu$ H, 181.26 $\mu$ H
Magnetizing Inductance $L_{m1}, L_{m2}$	1.41 mH, n/a, n/a	2.2 mH, 1.53 mH, 670 $\mu$ H	847 $\mu$ H, 423.5 $\mu$ H, 423.5 $\mu$ H
Peak magnetizing current at $f_s = f_r$	0.46A	0.22A	0.38A
Core of transformers $T, T_1, T_2$	PC95PQ50/50*2pcs ( $A_p=13\text{cm}^4$ ), n/a, n/a	n/a, PC95EE42/15 ( $A_p=9.7\text{cm}^4$ ), PC95PQ40/40( $A_p=6.6\text{cm}^4$ )	n/a, PC95PQ40/40( $A_p=6.6\text{cm}^4$ ), PC95PQ40/40 ( $A_p=6.6\text{cm}^4$ )
Resonant Capacitor $C_r, C_{r1}, C_{r2}$	5.45 nF, n/a, n/a	6.34nF, n/a, n/a	12.41nF, 24.82nF, 24.82nF
Peak voltage of $C_r$	1050V	880V	450 V
Primary switches	SPW35N60C3*4pcs	SPW35N60C3*4pcs+ IPP600N25N3G*2pcs	IPP600N25N3G *4pcs+ SPW35N60C3*2pcs
Secondary diodes/switches	IPP200N15N3G *4pcs	STPS61150C *8pcs	IPP200N15N3G *6pcs
Device counts	Least	Most	Less
Power density	High	Low	Medium

TABLE VI  
COST COMPARISON OF THE PROPOSED CONVERTER WITH THE OTHER CONVERTERS FOR TOPOLOGY CONFIGURATION

Component	Part Number	Rating	Unit Price (\$)	[35]	[37]	Proposed
MOSFET	Primary SPW35N60C3	650V, 35A	9.53	4	4	2
	Secondary IPP600N25N3G	250V, 25A	2.68	-	2	4
Diode	IPP200N15N3G	150V, 50A	2.75	4	-	6
	STPS61150C	150V, 60A	4.11	-	8	-
Total cost (\$)				49.12	76.36	46.28

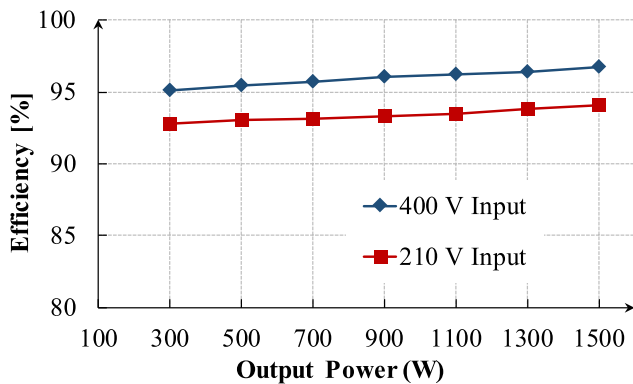


Fig. 25. Efficiency curve of the proposed LLC converter.

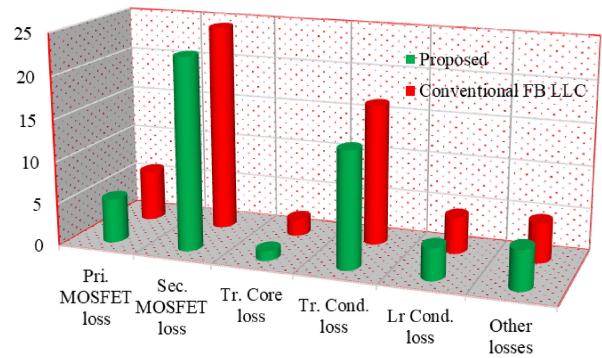


Fig. 26. Power loss comparison between the proposed converter and the conventional FB LLC converter.

## VIII. CONCLUSION

In this article, a novel dual LLC resonant converter is proposed employing an improved VFPSM-ZCC. The operation principle and detailed analysis are presented. The modified six switch H-bridge on the inverter side reduces the voltage stress to half of the input voltage, which is maintained for all load conditions. Moreover, the bridge configuration enables the converter to be operated at higher power ratings. The improved modulation scheme makes the converter gain independent of load and inductor ratio values. The limited switching frequency range minimizes the complexity of parameter design. The chosen value of magnetizing inductance increases the ZVS range. Furthermore, the elimination of circulating current at all conditions especially at light-load condition results in improved performance of the converter as compared to the traditional DAB LLC converter. The performance of the proposed converter with the modulation scheme has been verified by a designed 1.5-kW prototype. These attractive features make the proposed converter a suitable choice for wide input voltage range in medium/high power applications.

## REFERENCES

- [1] D. Sha, F. You, and X. Wang, "A high-efficiency current-fed semi-dual-active bridge DC-DC converter for low input voltage applications," *IEEE Trans. Ind. Electron.*, vol. 63, no. 4, pp. 2155–2164, Apr. 2016.
- [2] H. Zhou and A. M. Khambadkone, "Hybrid modulation for dual-active-bridge bidirectional converter with extended power range for ultracapacitor application," *IEEE Trans. Ind. Appl.*, vol. 45, no. 4, pp. 1434–1442, Jul./Aug. 2009.
- [3] A. K. Jain and R. Ayyanar, "PWM control of dual active bridge: Comprehensive analysis and experimental verification," *IEEE Trans. Power Electron.*, vol. 26, no. 4, pp. 1215–1227, Apr. 2011.
- [4] H. Xiao and S. Xie, "A ZVS bidirectional DC-DC converter with phase-shift plus PWM control scheme," *IEEE Trans. Power Electron.*, vol. 23, no. 2, pp. 813–823, Mar. 2008.
- [5] C.-S. Wang, S. Zhang, Y. Wang, B. Chen, and J. Liu, "A 5-kW isolated high voltage conversion ratio bidirectional CLTC resonant DC-DC converter with wide gain range and high efficiency," *IEEE Trans. Power Electron.*, vol. 34, no. 1, pp. 340–355, Jan. 2019.
- [6] M. Yaqoob, K. H. Loo, and Y. M. Lai, "Extension of soft-switching region of dual-active-bridge converter by a tunable resonant tank," *IEEE Trans. Power Electron.*, vol. 32, no. 12, pp. 9093–9104, Dec. 2017.
- [7] H. Park, M. Kim, and J. Jung, "Investigation of zero voltage switching capability for bidirectional series resonant converter using phase-shift modulation," *IEEE Trans. Power Electron.*, vol. 34, no. 9, pp. 8842–8858, Sep. 2019.
- [8] X. Li and A. K. S. Bhat, "Analysis and design of high-frequency isolated dual-bridge series resonant DC/DC converter," *IEEE Trans. Power Electron.*, vol. 25, no. 4, pp. 850–862, Apr. 2010.
- [9] T. Jiang, J. Zhang, X. Wu, K. Sheng, and Y. Wang, "A bidirectional LLC resonant converter with automatic forward and backward mode transition," *IEEE Trans. Power Electron.*, vol. 30, no. 2, pp. 757–770, Feb. 2015.
- [10] J.-H. H. Jung, H.-S. S. Kim, M.-H. H. Ryu, and J.-W. W. Baek, "Design methodology of bidirectional CLLC resonant converter for high-frequency isolation of DC distribution systems," *IEEE Trans. Power Electron.*, vol. 28, no. 4, pp. 1741–1755, Apr. 2013.
- [11] W. Sun, Y. Xing, H. Wu, and J. Ding, "Modified high-efficiency LLC converters with two split resonant branches for wide input-voltage range applications," *IEEE Trans. Power Electron.*, vol. 33, no. 9, pp. 7867–7879, Sep. 2018.
- [12] X. Sun, Y. Shen, Y. Zhu, and X. Guo, "Interleaved boost-integrated LLC resonant converter with fixed-frequency PWM control for renewable energy generation applications," *IEEE Trans. Power Electron.*, vol. 30, no. 8, pp. 4312–4326, Aug. 2015.
- [13] Y. Jeong, J.-K. Kim, J.-B. Lee, and G.-W. Moon, "An asymmetric half-bridge resonant converter having a reduced conduction loss for DC/DC power applications with a wide range of low input voltage," *IEEE Trans. Power Electron.*, vol. 32, no. 10, pp. 7795–7804, Oct. 2017.
- [14] S. M. S. I. Shakib and S. Mekhilef, "A frequency adaptive phase shift modulation control based LLC series resonant converter for wide input voltage applications," *IEEE Trans. Power Electron.*, vol. 32, no. 11, pp. 8360–8370, Nov. 2017.
- [15] T. Jiang, J. Zhang, X. Wu, K. Sheng, and Y. Wang, "A bidirectional three-level LLC resonant converter with PWAM control," *IEEE Trans. Power Electron.*, vol. 31, no. 3, pp. 2213–2225, Mar. 2016.
- [16] Z. Liang, R. Guo, J. Li, and A. Q. Huang, "A high-efficiency PV module-integrated DC/DC converter for PV energy harvest in FREEDM systems," *IEEE Trans. Power Electron.*, vol. 26, no. 3, pp. 897–909, Mar. 2011.
- [17] H. Wu, Y. Li, and Y. Xing, "LLC resonant converter with semiactive variable-structure rectifier (SA-VSR) for wide output voltage range application," *IEEE Trans. Power Electron.*, vol. 31, no. 5, pp. 3389–3394, May 2016.
- [18] M. Shang, H. Wang, and Q. Cao, "Reconfigurable LLC topology with squeezed frequency span for high-voltage Bus-Based photovoltaic systems," *IEEE Trans. Power Electron.*, vol. 33, no. 5, pp. 3688–3692, May 2018.
- [19] L. Costa, G. Buticchi, and M. Liserre, "A fault-tolerant series-resonant DC-DC converter," *IEEE Trans. Power Electron.*, vol. 32, no. 2, pp. 900–905, Feb. 2017.
- [20] X. Sun, X. Li, Y. Shen, B. Wang, and X. Guo, "Dual-bridge LLC resonant converter with fixed-frequency PWM control for wide input applications," *IEEE Trans. Power Electron.*, vol. 32, no. 1, pp. 69–80, Jan. 2017.
- [21] H. Wang and Z. Li, "A PWM LLC type resonant converter adapted to wide output range in PEV charging applications," *IEEE Trans. Power Electron.*, vol. 33, no. 5, pp. 3791–3801, May 2018.
- [22] Y. Jang, M. M. Jovanovic, J. M. Ruiz, and G. Liu, "Series-resonant converter with reduced-frequency-range control," in *Proc. IEEE Appl. Power Electron. Conf. Expo.*, 2015, pp. 1453–1460.
- [23] G. G. Oggier, G. O. Garcia, and A. R. Oliva, "Modulation strategy to operate the dual active bridge DC-DC converter under soft switching in the whole operating range," *IEEE Trans. Power Electron.*, vol. 26, no. 4, pp. 1228–1236, Apr. 2011.
- [24] B. Zhao, Q. Song, and W. Liu, "Efficiency characterization and optimization of isolated bidirectional DC-DC converter based on dual-phase-shift control for DC distribution application," *IEEE Trans. Power Electron.*, vol. 28, no. 4, pp. 1711–1727, Apr. 2013.
- [25] C. Mi, H. Bai, C. Wang, and S. Gargies, "Operation, design and control of dual H-bridge-based isolated bidirectional DC-DC converter," *IET Power Electron.*, vol. 1, no. 4, pp. 507–517, Dec. 2008.
- [26] F. Krismer, S. Round, and J. W. Kolar, "Performance optimization of a high current dual active bridge with a wide operating voltage range," in *Proc. 37th IEEE Annu. Power Electron. Specialists Conf.*, 2006, pp. 1–7.
- [27] H. Bai and C. Mi, "Eliminate reactive power and increase system efficiency of isolated bidirectional dual-active-bridge DC-DC converters using novel dual-phase-shift control," *IEEE Trans. Power Electron.*, vol. 23, no. 6, pp. 2905–2914, Nov. 2008.
- [28] G. Guidi, M. Pavlovsky, A. Kawamura, T. Imakubo, and Y. Sasaki, "Improvement of light load efficiency of dual active bridge DC-DC converter by using dual leakage transformer and variable frequency," in *Proc. IEEE Energy Convers. Congr. Expo.*, 2010, pp. 830–837.
- [29] B. Zhao, Q. Yu, and W. Sun, "Extended-phase-shift control of isolated bidirectional DC-DC converter for power distribution in microgrid," *IEEE Trans. Power Electron.*, vol. 27, no. 11, pp. 4667–4680, Nov. 2012.
- [30] V. Karthikeyan and R. Gupta, "Zero circulating current modulation for isolated bidirectional dual-active-bridge DC-DC converter," *IET Power Electron.*, vol. 9, no. 7, pp. 1553–1561, Jun. 2016.
- [31] S. Kulasekaran and R. Ayyanar, "Analysis, design, and experimental results of the semidual-active-bridge converter," *IEEE Trans. Power Electron.*, vol. 29, no. 10, pp. 5136–5147, Oct. 2014.
- [32] Y. A. Harrye, K. H. Ahmed, G. P. Adam, and A. A. Aboushady, "Comprehensive steady state analysis of bidirectional dual active bridge DC/DC converter using triple phase shift control," in *Proc. 23rd IEEE Int. Symp. Ind. Electron.*, 2014, pp. 437–442.
- [33] X. Li, "A LLC-Type dual-bridge resonant converter: Analysis, design, simulation, and experimental results," *IEEE Trans. Power Electron.*, vol. 29, no. 8, pp. 4313–4321, Aug. 2014.
- [34] J. W. Baek, D.-W. Yoo, and H.-G. Kim, "High-voltage switch using series-connected IGBTs with simple auxiliary circuit," *IEEE Trans. Ind. Appl.*, vol. 37, no. 6, pp. 1832–1839, Nov./Dec. 2001.
- [35] W. M. Dos Santos, M. S. Ortmann, R. Schweitzer, S. A. Mussa, and D. C. Martins, "Design and conception of a DAB converter (Dual Active Bridge) using the gyrators theory," in *Proc. 11th Brazilian Power Electron. Conf.*, 2011, pp. 359–364.

- [36] Z. Li, B. Xue, and H. Wang, "An interleaved secondary-side modulated LLC resonant converter for wide output range applications," *IEEE Trans. Ind. Electron.*, vol. 67, no. 2, pp. 1124–1135, Feb. 2020.
- [37] H. Hu, X. Fang, F. Chen, Z. J. Shen, and I. Batarseh, "A modified high-efficiency LLC converter with two transformers for wide input-voltage range applications," *IEEE Trans. Power Electron.*, vol. 28, no. 4, pp. 1946–1960, Apr. 2013.
- [38] G. Yang, P. Dubus, and D. Sadarnac, "Double-phase high-efficiency, wide load range high-voltage/low-voltage LLC DC/DC converter for electric/hybrid vehicles," *IEEE Trans. Power Electron.*, vol. 30, no. 4, pp. 1876–1886, Apr. 2015.
- [39] C. Li, M. Zhou, and H. Wang, "An H5-Bridge based asymmetric; LLC resonant converter with an ultra-wide output voltage range," *IEEE Trans. Ind. Electron.*, vol. 67, no. 11, pp. 9503–9514, Nov. 2020.



**Asif Mustafa** was born in Varanasi, India, in 1994. He received the bachelor's degree in electrical engineering from Aligarh Muslim University, India, Aligarh, Uttar Pradesh, in 2016. He is currently working toward the master's degree with the Power Electronics and Renewable Energy Research Laboratory (PEARL), University of Malaya, Kuala Lumpur, Malaysia.

His main research interests include bidirectional dc–dc converters for energy storage systems and their modulation techniques.



**Saad Mekhilef** (Senior Member, IEEE) received the bachelor's degree from the University of Setif, Setif, Algeria, in 1995, and the M.Sc. and Ph.D. degrees from the University of Malaya, Kuala Lumpur, Malaysia, in 1998 and 2003, respectively, all in electrical engineering.

He is currently a Professor and the Director of the Power Electronics and Renewable Energy Research Laboratory with the Department of Electrical Engineering, University of Malaya. He is also currently the Dean of the Faculty of Engineering, University of

Malaya. He is a Distinguished Adjunct Professor with the School of Software and Electrical Engineering, Faculty of Science, Engineering and Technology, Swinburne University of Technology, Melbourne, VIC, Australia. He has authored or coauthored more than 500 publications in international journals and conference proceedings. His current research interests include power converter topologies, control of power converters, renewable energy, and energy efficiency.

Dr. Mekhilef is serving as an Editor for *Renewable and Sustainable Energy Reviews*, an Associate Editor for *IEEE TRANSACTIONS ON POWER ELECTRONICS*, *IEEE OPEN JOURNAL OF INDUSTRIAL ELECTRONICS*, and *Journal of Power Electronics*.